metals

Article

Numerical Modeling of Electromagnetic Field Influences on Fluid Thermodynamic Behavior and Grain Growth During Solidification of 316L Stainless Steel Laser-Welded Plates

Zhengwei Zhang [1,*], Xinyuan Xu [1], Peng Ge [2,3] and Kai Li [1]

[1] China Ship Scientific Research Center, Wuxi 214000, China; xuxinyian@cssrc.com.cn (X.X.); likai@cssrc.com.cn (K.L.)
[2] College of Civil Engineering and Architecture, Henan University of Technology, Zhengzhou 450001, China; gp101022@haut.edu.cn
[3] Zhengzhou Research Institute of Mechanical Engineering Co., Ltd., Zhengzhou 450052, China
* Correspondence: zhangzw@cssrc.com.cn

Abstract: In the present study, a thermal–electromagnetic hydrodynamics model has been used to study welding temperature and melt flow characteristics during the laser welding of 316L steel. This welding was performed using an assisted electromagnetic field. In addition, a Monte Carlo model was used to study grain growth during solidification with the purpose of achieving a better understanding of the control of the microstructure. Based on the numerical model, which has been validated by experimental data, the effects of the current intensity of the electromagnetic field on the temperature distribution, melt flow characteristics, and grain growth are discussed here in detail. The simulation results showed that both Marangoni convection and welding temperature could be controlled by the magnetic damping effect, and that they increased due to the electromagnetic heating effect when using an electromagnetic field. Furthermore, when controlling the temperature distribution and melt flow velocity in the laminar flow of the melt pool, which was assisted by a 30 A current intensity of the electromagnetic field, the temperature gradient decreased by 13.5%. This decrease could be even larger than 50% when a turbulent flow was formed in the melt pool, which has here been demonstrated for a current intensity of 100 A. In addition, undercooling was found to decrease because of the increase in the melt flow velocity when using an assistive electromagnetic field. This led to a longer nucleation time in the melt pool. Furthermore, more and larger directional columnar grains, grown by the driving force of the temperature gradient, could be formed after the consumption of the small, nucleated grains near the solid–liquid interface. In short, by controlling the temperature distribution and melt flow velocity, the required grain morphology (equiaxed or columnar) and dimension (radius, length, or width) can be controlled by coarsening and epitaxial growth.

Keywords: melt flow; heat transfer; electromagnetic field; laser welding

check for updates

Academic Editor: Hardy Mohrbacher

Received: 8 April 2025
Revised: 8 May 2025
Accepted: 26 May 2025
Published: 28 May 2025

Citation: Zhang, Z.; Xu, X.; Ge, P.; Li, K. Numerical Modeling of Electromagnetic Field Influences on Fluid Thermodynamic Behavior and Grain Growth During Solidification of 316L Stainless Steel Laser-Welded Plates. *Metals* **2025**, *15*, 609. https://doi.org/10.3390/met15060609

Copyright: © 2025 by the authors. Licensee MDPI, Basel, Switzerland. This article is an open access article distributed under the terms and conditions of the Creative Commons Attribution (CC BY) license (https://creativecommons.org/licenses/by/4.0/).

1. Introduction

With its characteristics of high efficiency, capacity for automation, and precision, laser welding is a popular joining technology for stainless steel [1–4]. Laser energy absorption efficiency can be greatly increased by the formation of a keyhole during deep penetration laser welding, which leads to increased manufacturing efficiency [5,6]. However, the extremely high temperature at the center of the melt pool leads to the fluctuation and

collapse of the keyhole, which is a key factor in the formation of pores or defects in the manufactured structure [7–9]. In addition, the large temperature gradient in the melt pool leads to the fast growth of directional columnar grains. Therefore, the mechanical properties of the laser welding joint can be largely decreased by the inhomogeneous temperature distribution in the melt pool [7,10–12].

In recent years, electromagnetic fields have frequently been used in laser welding/additive manufacturing. They effectively influence thermodynamic behavior in the melt pool [13–16] by the magnetic damping/thermoelectric magnetic effect [17–27]. Welding stability [18,19], porosity [20], residual stress [21], and microstructure [22,23] can all be effectively controlled using different assistive electromagnetic fields. On the one hand, the magnetic damping effect can be used to suppress the high velocity of Marangoni convection, with the object of accelerating heat and mass transfer for the active control of element segregation in the melt pool. On the other hand, the flow of molten material during the rapid cooling process can be influenced by the thermoelectric magnetic effect, which is important for an increase in the solidification rate and, thus, control of grain morphology [28]. Shuai et al. [29] added a transverse static magnetic field to the Al-12% Si laser additive manufacturing process. By using a thermoelectric magnetic force of 10^5 N/m^3 on the dendrites, which was caused by a static magnetic field of 0.35 T, the Marangoni convection in the melt pool wasclearly suppressed. This resulted in a decrease in the high temperature gradient. By using a static magnetic field, Nie et al. [30] successfully reduced residual stress by 20% (from 392.5 MPa to 315.45 MPa) in a laser-remelted Inconel 718 superalloy. To better understand the mechanism behind the effect of the assistive magnetic field on the heat and mass transfer in the melt pool, Wang et al. [31] used a thermal–electromagnetic hydrodynamic model when studying thermodynamic behavior variations in the melt pool (such as Marangoni convection and keyhole fluctuations) with different electromagnetic fields. The results indicated that the Lorentz force, which was provided by the electromagnetic field, reached its peak at the bottom of the molten pool. It could effectively suppress Marangoni convection on the surface of the molten pool, promote backflow at the bottom of the molten pool, and aid in the suppression of the fluid spiral rotation behind the keyhole wall. Thus, it improved the stability of the keyhole wall of the molten pool. Furthermore, Zeng et al. [32] changed the static magnetic field into a pulsed one in a systematic study of the influence of magnetic field parameters on molten flow in laser additive manufacturing. The numerical results showed that pulsed magnetic fields could effectively increase the flow velocity in the molten material, thereby largely decreasing the maximum temperature. Similar conclusions were obtained by Deng et al. [25] and Zhang [27].

However, some problems were found (including an increase in the temperature gradient near the boundary of the melt pool and an increase in molten flow fluctuation) when an electromagnetic field was used to improve the characteristics of the thermodynamic behavior in the melt pool. Therefore, further research is necessary on the control of the temperature gradient and stability of the molten flow, which are key factors for the comprehensive improvement of thermodynamic behavior and grain growth during solidification in electromagnetic field-assisted laser welding/additive manufacturing. The purpose is then to obtain a laser metallurgy manufacturing product with lower thermal stress, better grain morphology, and smaller pose/defect.

In the present study, a thermal–electromagnetic hydrodynamic model has been used in a systematic study of the effects of electromagnetic field parameters on the heat transfer and molten flow characteristics in a melt pool. Based on the simulation results of the temperature gradient, melt flow velocity, and cooling rate, the grain growth during solidification of the 316L steel plate melt was simulated using the Monte Carlo model. The purpose was

to achieve a better understanding of the control of the microstructure and the mechanical properties of the laser-welded product.

2. Experiment

We conducted a laser welding experiment by building a laser welding system with an electromagnetic field. The laser, with 600–3000 W power and a frequency of 1080 nm, was set up with a multi-axis mechanical arm, as shown in Figure 1. The 316L steel sample, with a size of 150 × 75 × 1.5 mm, was welded using the manufacturing parameters shown in Table 1. The electromagnetic field generator was set on the side of the welded sample. When the coil in the electromagnetic field generator was powered on with different current intensities, magnetic fields with different magnetic induction intensities around the welded sample were generated to apply the Lorentz force to the melt pool. In addition, two high-speed cameras were set up to measure the welding temperature and shape of the melt pool.

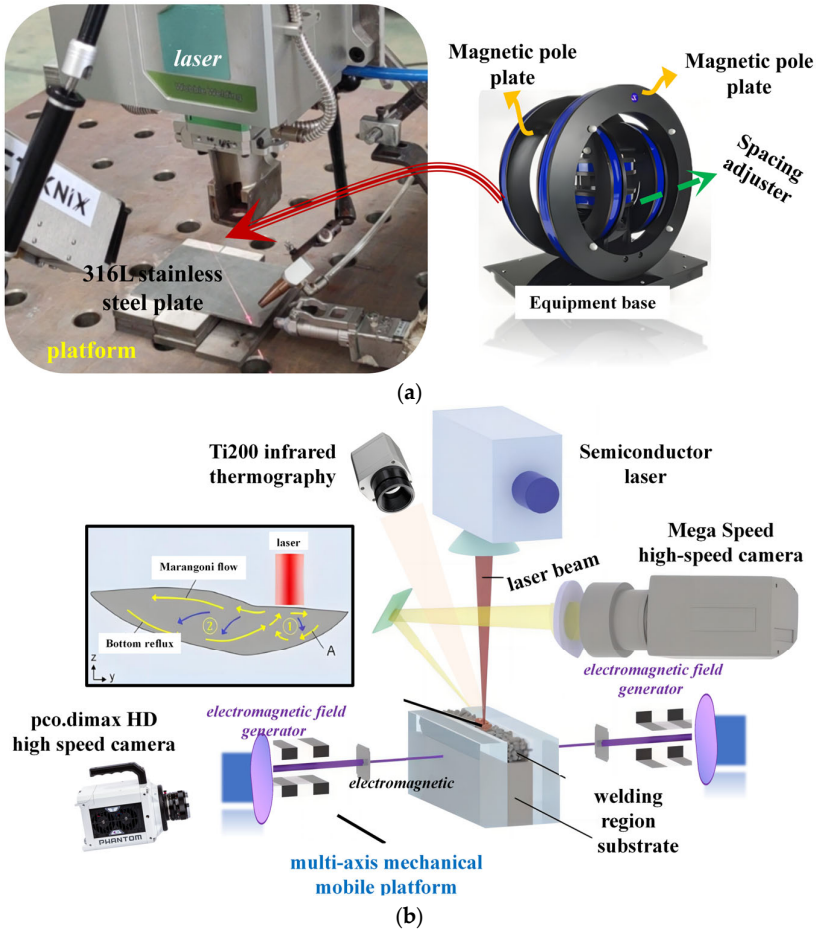


Figure 1. The built laser welding system with electromagnetic field: (**a**) electromagnetic-field-assisted laser welding equipment; (**b**) schematic diagram of the electromagnetic-field-assisted laser welding system.

Table 1. Manufacturing parameters in the electromagnetic-field-assisted laser welding of 316L steel.

Manufacturing Parameters	Value
Laser power, Q/(W)	1000
Scanning speed, v/(mm/s)	10
Laser beam diameter, d/(mm)	2
Current intensity, I/(A)	30/50/80/100/120/150/200

3. Numerical Model

In this paper, a thermal–electromagnetic hydrodynamics model was used to study the heat and mass transfer process in the melt pool during the laser welding of 316L steel samples. First, the liquid metal flow in the melt pool was assumed to be Newtonian, laminar, and incompressible [9]. Then, when the Reynolds number was increased with the molten flow velocity, the RNG κ-ε model was used to consider the influence of turbulent flow on the simulation results in the VOF model. The Boussinesq approximation was used to consider the effect of temperature-dependent density on flow characteristics [33]. In particular, the error of the numerical results simulated by the proposed model in this paper was related to some process and environmental conditions; this is important for the formation of pores or defects in the melt pool, which can greatly influence the molten flow characteristics and velocity, and thus the heat transfer and temperature distribution in the melt pool. In this paper, the material was assumed to be isotropically homogeneous [34]. No pores or defects form in the melt pool.

The temperature-dependent thermal properties of 316L steel are listed in Table 2 [35], and the temperature-dependent viscosities are listed in Table 3 [36]. To study the thermodynamic behaviors in the stable melt pool, a local region in the experimental sample, with a size of 20 × 10 × 1.5 mm, was chosen as the simulation domain, as shown in Figure 2. The general software COMSOL Multiphysics 6.2 was used to calculate the temperature and melt flow velocity in the electromagnetic-field-assisted laser welding of 316L steel. When the mesh size is changed from 0.01 mm to 0.2 mm, the simulation can be finished with a small calculation error, but with different calculation times. In the current work, the mesh size was chosen as 0.05 mm. There are 51,840 cells in the solid and liquid domains, with 86,400 in the air domain.

Table 2. Temperature-dependent thermal properties of 316L steel [35].

Temperature K	Density /(kg/m^3)	Thermal Conductivity W/(m·K)	Heat Specific J/(kg·K)
293.15	7979	13.31	470
373.15	7937	14.68	487
773.15	7760	20.96	571
1273.15	7535	27.53	676
1473.15	7430	29.76	719
1673.15	7320	31.95	765
1773.15	7320	320	765

Table 3. Temperature-dependent viscosity of 316L steel [36].

Temperature K	1739.13	1891.3	2072.46	2246.38	2442.03	2615.94	2789.86
Viscosity Kg/ms	0.0072	0.0057	0.0044	0.0035	0.003	0.0025	0.0022

In the current model, the governing equations for molten flow can be written as [37]:
The mass equation:

$$\frac{\partial \rho}{\partial t} + \nabla \cdot (\rho \cdot \mathbf{v}) = 0 \quad (1)$$

The momentum equation:

$$\rho\left(\frac{\partial \mathbf{v}}{\partial t} + \mathbf{v} \cdot \nabla \mathbf{v}\right) = -\nabla P + \mu \nabla^2 \mathbf{v} - \frac{\mu}{K} \cdot \mathbf{v} + \beta \rho \cdot \mathbf{g} \cdot (T - T_{\mathrm{ref}}) + S_m \quad (2)$$

The energy equation:

$$\frac{\partial(\rho H)}{\partial t} + \mathbf{v} \cdot \nabla(\rho H) = \nabla \cdot (k \cdot \nabla T) + S_v \tag{3}$$

where ρ, k, and β are the density, thermal conductivity, and thermal expansion coefficient of 316L steel, respectively, t is the simulation time, $\mathbf{v}$ is the velocity vector, $\mathbf{g}$ is the gravity vector, P is pressure, K is the drag coefficient, T is the temperature, T_{ref} is the reference temperature, H is the enthalpy, and S_{m} and S_{v} are the momentum and energy source terms, respectively. The latent heat in melting is 256,400 J/kg with a liquidus temperature of 1723.15 K and a solidus temperature of 1673.15 K.

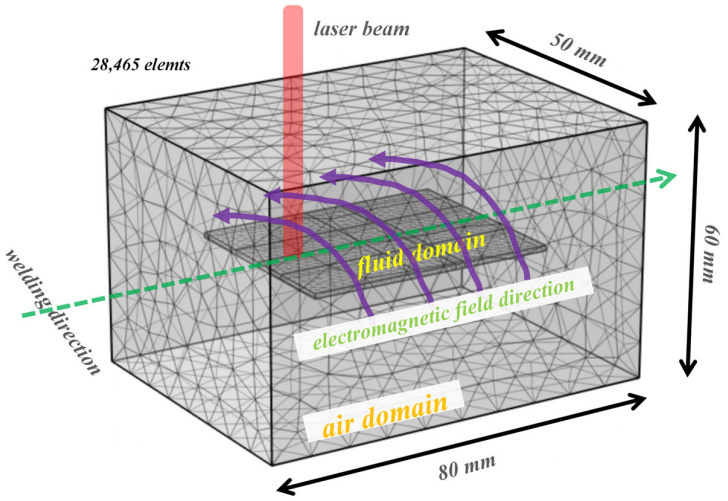


Figure 2. The thermal–electromagnetic hydrodynamics model with electromagnetic field.

The volume of fluid (VOF) method is used in the modeling; its equation can be written as [38]:

$$\frac{\partial F}{\partial t} + \nabla \cdot (F \cdot \mathbf{v}) = 0 \tag{4}$$

where F is the volume fraction of the cell, which has a value between 0 and 1. The energy balance equation is given by [1]:

$$k\frac{\partial T}{\partial \mathbf{n}} = q_{\mathrm{inp}} - q_{\mathrm{eva}} - q_{\mathrm{conv}} - q_{\mathrm{rad}} \tag{5}$$

where q_{inp} is the laser heat input and q_{eva} is heat loss by evaporation. In works by other researchers, such as Zhou et al. [39] and Ross et al. [40], a double ellipsoid heat source was used to model the heat energy distribution of the laser beam. The welding temperature can agree well with the experimentally measured data. It is true that the use of the double ellipsoid may lead to an error in the simulation of the laser welding temperature, but the error is small, commonly less than 10%. Therefore, in this paper, based on the research mentioned above, the double ellipsoid heat source model was chosen. It can be written as [39,40]

$$q_{\mathrm{f}} = \frac{6\sqrt{3}\eta_{\mathrm{s}} Q f_{\mathrm{f}}}{a_{\mathrm{f}} bc\pi\sqrt{\pi}} \exp\left\{-3\left[\left(\frac{x+v_1 t}{a_{\mathrm{f}}}\right)^2 + \left(\frac{y}{b}\right)^2 + \left(\frac{z}{c}\right)^2\right]\right\} \tag{6}$$

for the front part, and

$$q_{\mathrm{r}} = \frac{6\sqrt{3}\eta_{\mathrm{s}} Q f_{\mathrm{r}}}{a_{\mathrm{r}} bc\pi\sqrt{\pi}} \exp\left\{-3\left[\left(\frac{x+v_1 t}{a_{\mathrm{r}}}\right)^2 + \left(\frac{y}{b}\right)^2 + \left(\frac{z}{c}\right)^2\right]\right\} \tag{7}$$

for the rear part. a_f, a_r, b, and c are the sizes along the X, Y, and Z directions, respectively, f_f and f_r are the heat-input coefficients of the two semi-ellipsoids, η_s is the absorption coefficient, Q is the laser power, v_l is the moving speed of laser, and t is the welding time.

When the coil in the electromagnetic field generator is powered on with different direct current intensities, the magnetic induction intensities generated around the welded sample can be solved using Maxwell's equations:

$$\nabla \times \mathbf{E} = -\frac{\partial \mathbf{B}}{\partial t} \tag{8}$$

$$\nabla \times \mathbf{B} = \mu_0 \mathbf{J}_{\text{melt}} + \mu_0 \varepsilon_0 \frac{\partial \mathbf{E}}{\partial t} \tag{9}$$

where $\mathbf{E}$ is electric field intensity, $\mathbf{B}$ is magnetic field intensity, $\mathbf{J}_{\text{melt}}$ is induced current, and μ_0 and ε_0 are the permeability of vacuum and electrical conductivity of the material, respectively.

Given the generated magnetic field and induced electric field, the induced current in the melt pool can be found. Then, the Lorentz force, $\mathbf{F}_L$, in the momentum source term can be written as:

$$\mathbf{F}_L = \mathbf{J}_{\text{melt}} \times \mathbf{B} \tag{10}$$

When an electromagnetic field is used in laser welding, electromagnetic heating, q_{ele}, also needs to be considered in Equation (5), which can be written as [14]:

$$q_{ele} = \left| \vec{J} \right|^2 / \sigma \tag{11}$$

With the increase in molten flow velocity, electromagnetic heating caused by the induced current within the melt flow is greatly increased. As a result, if the flow velocity of melt material is large enough during welding, the main heating source in electromagnetic-field-assisted laser welding will be changed from laser heating to electromagnetic heating.

In addition, the recoil pressure, P_{rec}, and the surface tension, σ_{sur}, are also considered in the numerical model; these can be written as, respectively [41,42]:

$$P_{rec} = 0.54 P_0 \exp\left[\frac{L_v}{R T_b}\left(1 - \frac{T_b}{T}\right)\right] \tag{12}$$

$$\sigma_{sur} = \sigma_0 + d\sigma/dT \cdot (T - T_l) \tag{13}$$

where L_v = 9.0 × 10^6 J/kg is the latent heat of evaporation at atmospheric pressure P_0, T_b = 3260 °C is the boiling temperature, σ_0 = 1.65 N/m is the surface tension at the liquidus temperature, $d\sigma/dT$ = −2.6 × 10^{-4} N/(m·°C), R = 8.314 J/(mol·°C) is the universal gas constant, and T_l is the liquidus temperature.

When the governing equations are solved, the boundary conditions, including the pressure outlets and wall boundaries, are needed. In this work, the top surface of the welding sample is set as the pressure outlet boundary, and the other surfaces are set as the wall boundaries. The boundary conditions can be written as [1]:

Pressure outlet boundary condition:

$$\begin{cases} P_{\text{outlet}} = P_0 \\ T_{\text{outlet}} = T_0 \end{cases} \tag{14}$$

Wall boundary condition:

$$\begin{cases} q_{\text{conv}} = h(T - T_0) \\ q_{\text{rad}} = \sigma\varepsilon\left(T^4 - T_0^4\right) \end{cases} \tag{15}$$

where P_0 and T_0 are the ambient pressure and temperature during MLS welding, respectively, q_{conv} and q_{rad} are the heat loss caused by heat convection and heat radiation, respectively, h is the heat convection coefficient, ε is the material radiation emissivity, and σ is the Stefan–Boltzmann constant.

Based on the electromagnetic-field-assisted laser welding temperature simulation results of 316L stainless steel plate, the modeling of grain growth in the solidification of the melt pool was carried out using the Monte Carlo (MC) method. In the MC model, the grain boundary energy can be calculated by the difference between the orientation number at the lattice site and the nearest neighbor lattice site, which can be written as [43]:

$$E = -J\sum_{j=1}^{m}\left(\delta_{S_i S_j} - 1\right) \tag{16}$$

where J is a positive constant that represents the grain-boundary energy, m is the total number of sites near the lattice point, δ is the Kronecker symbol, S_i is the orientation at a randomly selected site, and S_j represents the orientations of its nearest neighbors.

The probability of the energy change due to the attempted orientation can be written as:

$$p = \begin{cases} 1, & \Delta E \le 0 \\ e^{-\frac{\Delta E}{k_B T}} = e^{-\frac{(m_2 - m_1)J}{k_B T}} & \Delta E \ge 0 \end{cases} \tag{17}$$

where ΔE is the change in grain-boundary energy due to reorientation, k_{B} is the Boltzmann constant, T is the temperature, and m_1 and m_2 are the numbers of different orientations before and after reorientation.

The relationship between the Monte Carlo step (MCS) and real simulation time in the VOF model can be written as:

$$(\text{MCS})_{\Omega_1}^{(n'+1)^{n_1}} = \left(\frac{d_0}{K_1\lambda}\right)^{n'+1} + \frac{(n'+1)\alpha_{\text{mcs}} C_1^{n'}}{(K_1\lambda)^{n'+1}}\sum_{i=1}^{n_t}\left[\exp^{n}\left(-\frac{Q}{RT_{\Omega_1,i}}\right)\Delta t_{\Omega_1,i}\right] \tag{18}$$

where d_0 is the initial coarsening size, K_1 and n_1 are model constants calculated using regression analysis, Q is the activation energy, R is the gas constant, and α_{mcs} and n' are scale factors. Our early research into the numerical simulation of grain growth using the Monte Carlo model [44–46] showed the great influences of the calculation parameters K_1 and n_1 on final grain morphology and size. Here, using comparisons of the grain size with the experimental data, K_1 = 0.96 and n_1 = 1.05 are selected in this paper. In addition, because of the large size of the computational domain, the transverse cross section and grain growth direction are controlled by the gradient temperature [47]. With the different thermal histories of each point in the cross section, the different MCSs in each lattice can be calculated in a discrete form as follows:

$$(\mathbf{MCS}) = \begin{Bmatrix} \text{MCS}_{1,1} & \text{MCS}_{1,2} & \dots & \text{MCS}_{1,\tilde{m}} \\ \text{MCS}_{2,1} & \text{MCS}_{2,2} & \dots & \text{MCS}_{2,\tilde{m}} \\ \vdots & \vdots & \vdots & \vdots \\ \text{MCS}_{\tilde{n},1} & \text{MCS}_{\tilde{n},2} & \dots & \text{MCS}_{\tilde{n},\tilde{m}} \end{Bmatrix} \tag{19}$$

When the MCS data is normalized over the cross section, the uniform format for the MCS can be obtained by $MCS_{\tilde{n},\tilde{m}}/MCS_{\max} = \zeta_{\tilde{n},\tilde{m}}$

$$\mathbf{MCS}_{(\tilde{n},\tilde{m})} = \begin{Bmatrix} MCS_{1,1}\cdot\zeta_{1,1} & MCS_{1,2}\cdot\zeta_{1,2} & \cdots & MCS_{1,m^*}\cdot\zeta_{1,m^*} & \cdots & MCS_{1,\tilde{m}}\cdot\zeta_{1,\tilde{m}} \\ MCS_{2,1}\cdot\zeta_{2,1} & MCS_{2,2}\cdot\zeta_{2,2} & \cdots & MCS_{2,m^*}\cdot\zeta_{2,m^*} & \cdots & MCS_{2,\tilde{m}}\cdot\zeta_{2,\tilde{m}} \\ \vdots & \vdots & \cdots & \vdots & \cdots & \vdots \\ MCS_{n^*,1}\cdot\zeta_{n^*,1} & MCS_{n^*,2}\cdot\zeta_{n^*,2} & \cdots & MCS_{n^*,m^*} & \cdots & MCS_{n^*,\tilde{m}}\cdot\zeta_{n^*,\tilde{m}} \\ \vdots & \vdots & \cdots & \vdots & \cdots & \vdots \\ MCS_{\tilde{n},1}\cdot\zeta_{\tilde{n},1} & MCS_{\tilde{n},2}\cdot\zeta_{\tilde{n},2} & \cdots & MCS_{\tilde{n},m^*}\cdot\zeta_{\tilde{n},m^*} & \cdots & MCS_{\tilde{n},\tilde{m}}\cdot\zeta_{\tilde{n},\tilde{m}} \end{Bmatrix} \quad (20)$$

where n^* and m^* are the lattice site locations with the maximum MCS. In addition, because of the strong randomness in lattice site selection and orientation number updating in the traditional Monte Carlo grain growth model, it is difficult to consider the important influence of temperature distribution, especially temperature gradient, on grain growth in the solidification of the welded sample. Therefore, in this paper, the Monte Carlo grain growth model is improved by considering the calculated temperature gradient in the welded product. In the improved grain growth model, the probability of energy change, which is written in Equation (17), can be corrected as:

$$p_{\dot{T}} = p\cdot\cos\left(\left\langle\vec{n}_{\tau},\vec{n}_{\dot{T}}\right\rangle\right) = \begin{cases} \cos\left(\left\langle\vec{n}_{\tau},\vec{n}_{\dot{T}}\right\rangle\right) & \Delta E \le 0 \\ \cos\left(\left\langle\vec{n}_{\tau},\vec{n}_{\dot{T}}\right\rangle\right)\cdot e^{-\frac{(m_2-m_1)\cdot J}{k_B T}} & \Delta E > 0 \end{cases} \quad (21)$$

where $p_{\dot{T}}$ is the changing probability of the orientation number considering the temperature gradient, $\vec{n}_{\tau}$ is the direction vector from the current lattice site to the probably changed neighbor lattice site, $\vec{n}_{\dot{T}}$ is the direction vector of the temperature gradient in the current lattice site, and $\left\langle\vec{n}_{\tau},\vec{n}_{\dot{T}}\right\rangle$ is the angle between $\vec{n}_{\tau}$ and $\vec{n}_{\dot{T}}$, which can be written as:

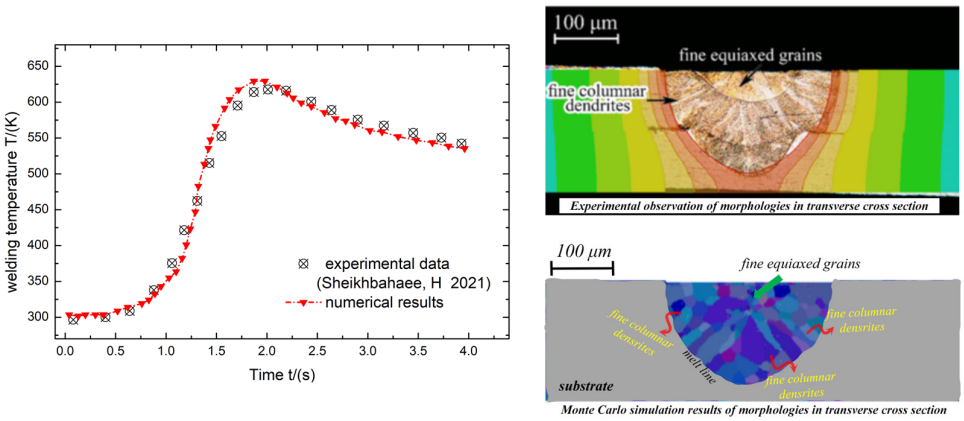
$$\vec{n}_{\dot{T}} = \left(\phi_{i,T\max}-\phi_i,\phi_{j,T\max}-\phi_j\right) \quad (22)$$

where $\left(\phi_{i,T_{\max}},\phi_{j,T_{\max}}\right)$ is the location of the lattice site with the maximum welding temperature, and $\left(\phi_i,\phi_j\right)$ is the location of the current lattice site. Using the improved Monte Carlo model, which considers the temperature gradient in heat transfer analysis, the highly random grain growth algorithm can be seen to be effectively driven by temperature distribution in the welding product.

4. Discussions

To validate the simulation results of the welding temperature distribution, melt flow characteristics, and grain growth during solidification, the welding process described in Ref. [48] has been repeated using the model proposed in the present study. A comparison between the experimental temperature and numerical results is presented in Figure 3a. By using the thermal–electromagnetic hydrodynamic model, the simulation error for the welding temperature was less than 10%. Thus, the simulation results agreed well with the experimental data. Thereafter, when the calculated temperature distribution was considered in the improved Monte Carlo grain growth model, a similar grain morphology could be found in the melt pool. The results of grain size comparisons between experimental and numerical data, which are listed in Table 4, show that the grain size errors of the equiaxed grains near the top and bottom of the melt pool are about 10%. The errors in the lengths and widths of columnar grains in the middle of the melt pool are 6% and 2%, respectively. Grain growth in laser welding can be well simulated using the Monte Carlo

model proposed in this paper. Therefore, the correctness of the microstructure modeling can be validated using the proposed Monte Carlo grain growth model.



(**a**) (**b**)

Figure 3. Validations of the thermal–electromagnetic hydrodynamics model and the Monte Carlo model: (**a**) validation of welding temperature calculated by the thermal–electromagnetic hydrodynamics model [48]; (**b**) validation of grain morphology in transverse cross-section simulated by the Monte Carlo model.

Table 4. Grain sizes in microstructure: Comparison between experimental and numerical.

Equiaxed Grains			**Columnar Grains**				
Num.	Exp. data 15	Num. data 17	Num.	Exp. data 11	Num. data 12	Num.	Exp. data 11	Num. data 12
Size (μm)	18.29	21.69	Length (μm)	64.47	45.64	Width (μm)	9.82	11.49
	12.84	16.62		53.33	58.03		7.95	27.04
	11.57	21.3		42.98	49.69		17.54	10.54
	24.56	9.95		80.24	94.5		13.15	22.22
	17.48	13.56		81.72	62.6		19.05	9.68
	7.59	14.03		53.26	72.94		22.2	34.25
	10.54	18.71		62.95	68.55		12.92	15.24
	11.95	15.88		63.04	68.85		13.34	18.27
	27.62	20.14		64.15	38.64		11.48	7.89
	13.28	21.96		71.05	64.61		23.68	9.37
	21.58	12.57		67.85	38.87		13.31	10.52
	10.85	20.9		-	54.95		-	12.4
	14.54	22.16		-	-		-	-
	11.58	20.57		-	-		-	-
	26.67	25.54		-	-		-	-
	-	13.94		-	-		-	-
	-	11.98		-	-		-	-
Mean Size (μm)	16.06	17.73	Mean length (μm)	64.09	59.82	Mean width (μm)	14.95	14.56

Based on the validated thermal–electromagnetic hydrodynamic model, the laser welding temperature and melt flow characteristics in the melt pool could be well simulated (Figure 4). When there was no assistive electromagnetic field in the laser welding of 316L steel plates, a maximum temperature of 2058.94 K could be achieved for the welding time of 3 s. Compared to the liquid temperature of the 316L steel, the much higher welding temperature led to a strong Marangoni convection on the top surface of the melt pool, with a value of 2.77 mm/s. Using an electromagnetic field with a current intensity of 30 A during laser welding, the strong Marangoni convection could be effectively constricted by

the magnetic damping effect (Figure 4b). For a welding time of 3 s, the Hartmann number *Ha* calculated by the following equation is 42.67. The maximum melt flow velocity on the top surface of the welded sample is decreased to 0.71 mm/s.

$$Ha = BL\sqrt{\sigma/\mu} \tag{23}$$

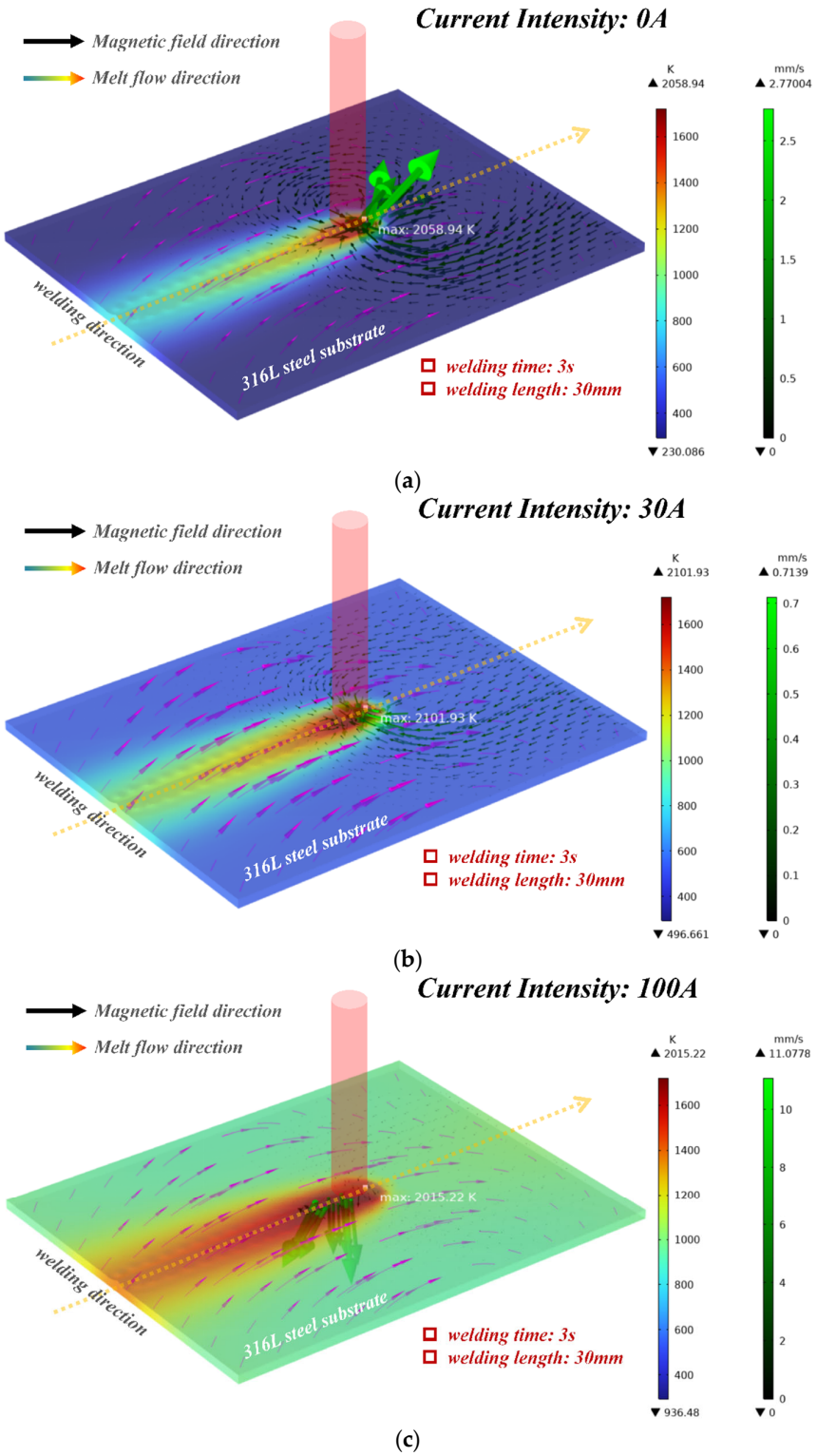


Figure 4. Laser welding temperatures and flow velocities in the melt pool with different current intensities of electromagnetic field: (**a**) current intensity of 0 A; (**b**) current intensity of 30 A; (**c**) current intensity of 100 A.

In addition, a much higher temperature could be achieved in both the 316L steel substrate and the melt pool. The heating temperature in the substrate then increased from 230.086 K to 496.661 K, and the maximum welding temperature increased from 2058.94 K to 2101.93 K in the melt pool. The additional heating by the electromagnetic field, which was similar to preheating, could effectively make the temperature distribution in the welded 316L steel sample uniform, thereby largely decreasing the temperature gradient (Figure 4b). Furthermore, when the current intensity of the electromagnetic field was increased to 100 A (*Ha* = 2.62), different melt flow characteristics and temperature distributions were found in the welded 316L steel sample. Induced by the strong electromagnetic field, the flow characteristics of the molten 316L steel, which were controlled by the Marangoni convection, were changed by the Lorentz force control. The maximum flow velocity in the melt pool was then increased to 11.08 mm/s, with a downward direction in the melt pool (Figure 4c). This could have caused an unstable turbulent flow in the melt pool. In addition, the electromagnetic heating effect was enhanced by the large current intensity in the electromagnetic field. The substrate was then heated to 936.48 K, while the maximum welding temperature in the melt pool was still about 2000 K. Although it is possible to effectively control the melt flow characteristics and temperature distribution in laser welding that uses an electromagnetic field, the control parameters need to be further designed to prevent the breakage of the laminar melt flow characteristics and the overheating of the substrate.

To further study the effect of the current intensity of the electromagnetic field on the thermal and flow characteristics in the laser welding of 316L steel, the melt flow velocities and welding temperatures have here been measured for different designed parameters of the electromagnetic field (Figure 5). When the current intensity of the electromagnetic field was increased from 0 A to 200 A, a large increase in the melt flow velocity could be observed at the measured point (from 6.42 mm/s to 26.5 mm/s). As shown in Figure 5a, this obvious change in melt flow velocity, which was driven by the change in flow characteristics from the Marangoni convection to the Lorentz force, was found between the current intensity of 30 A and 80 A. When the current intensity of the electromagnetic field was larger than 80 A, the melt flow characteristics, which were controlled by the Lorentz force, became complex and unstable. Also, the flow velocity curve was practically identical to the turbulent pulsation curve when the current intensity of the electromagnetic field was 200 A. In summary, for the laser welding of 316L steel, the use of an electromagnetic field with a current intensity lower than 30 A resulted in a well-controlled flow velocity in the melt pool, which was due to the magnetic damping effect. The purpose was to decrease the fast transfer of molten elements in the 316L steel and to homogenize the molten material. In addition, if fast cooling of the welded 316L steel was necessary for fast undercooling of the melt pool, the current intensity of the electromagnetic field could be chosen between 30 A and 100 A. However, the current intensity could not be further increased to prevent the formation of a turbulent flow in the melt pool.

The effect of electromagnetic field current intensity on the welding temperature is presented in Figure 5b. The electromagnetic heating effect increased with an increase in the current intensity, which resulted in an increased temperature of the welded 316L steel. For a current intensity of 30 A, and before the heating of the measuring point by the moving laser, an increase in temperature of 544.14 K was found at this measuring point. In the cooling process, a lower cooling rate was also found. In addition, increased electromagnetic field current intensity resulted in a higher preheating temperature and a lower cooling rate at the measuring point. Furthermore, for a current intensity of 200 A, the preheating temperature and maximum cooling rate were 1408.8 K and 311.9 K/s, respectively. It can be seen that the preheating temperature of 1408.8 K is almost the melting temperature

of 316L steel. In real applications of assistive electromagnetic fields in laser welding, the current intensity must be controlled to prevent overheating of the welded sample. This is to be compared with the initial temperature of 293.15 K and the maximum cooling rate of 823.8 K/s when no assistive electromagnetic field was used. It can be seen that, with the use of an assistive electromagnetic field, the laser welding of 316L steel could be performed at a higher initial temperature and a lower cooling rate. This was advantageous for the formation and growth of more equiaxial grains in the melt pool, thereby enhancing the mechanical properties of the welded 316L steel.

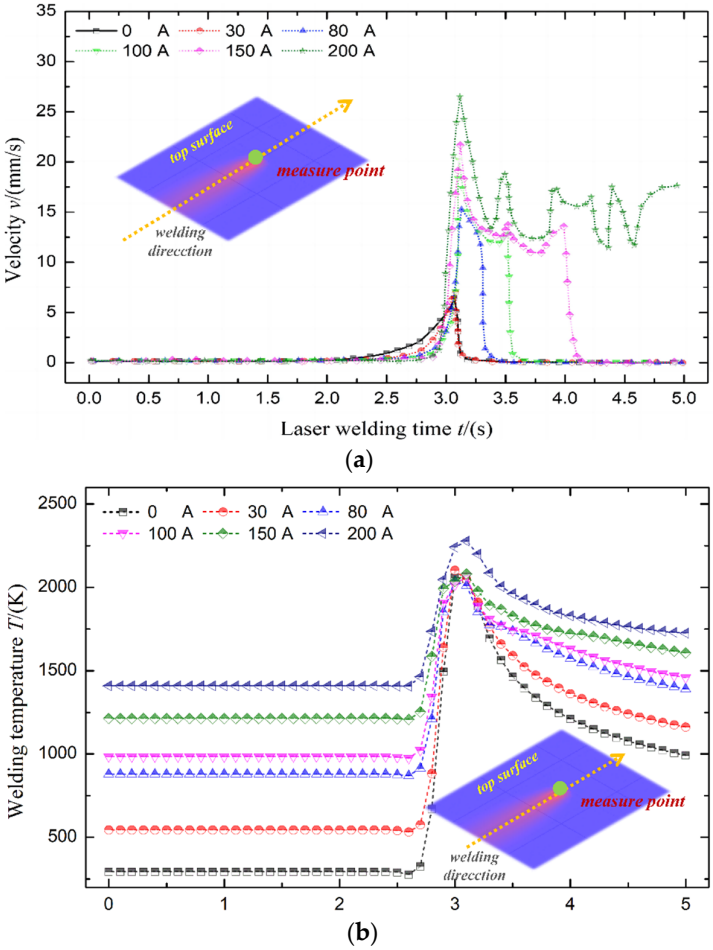


Figure 5. Temperature and flow velocity histories with different current intensities of electromagnetic field: (**a**) molten flow velocity histories with different current intensities; (**b**) welding temperature histories with different current intensities.

In addition, the temperature gradient, which is important for grain growth, was simulated using the thermal–electromagnetic hydrodynamic model. The temperature gradients in the transverse and longitudinal cross-sections are presented in Figures 6 and 7, respectively. With an increase in the current intensity of the applied assistive electromagnetic field, the temperature gradient in the transverse cross section decreased greatly (Figure 6). The maximum temperature gradient could then decrease from 1012.76 K/mm (without the electromagnetic field) to 317.8 K/mm (with a current intensity of 200 A). In addition, the location of the maximum temperature gradient moved further away from the center of the melt pool. When the current intensity of the electromagnetic field was 0 A, the distance from the maximum temperature gradient to the center line of the laser was 1.75 mm. It increased to 3.74 mm when the current intensity increased to 200 A. Similar to the temperature gradient in the transverse cross-section, a decreased temperature gradient was

found in the longitudinal cross section with an increase in the current intensity of the electromagnetic field. For a current intensity of 0 A and without an assistive electromagnetic field, the maximum temperature gradient in the melt pool became 939.2 K/mm (Figure 7). When an electromagnetic field with a current intensity of 30 A was used for 316L steel welding, the maximum temperature gradient clearly decreased by 13.5%. When the current intensity increased to 100 A, the maximum temperature gradient decreased by 51%. It was also found that the temperature distribution in the welded 316L steel became more uniform with the use of an electromagnetic field. The much smaller temperature gradient in both the transverse and longitudinal cross sections was advantageous for the relaxation of thermal stress and the growth of equiaxial grains.

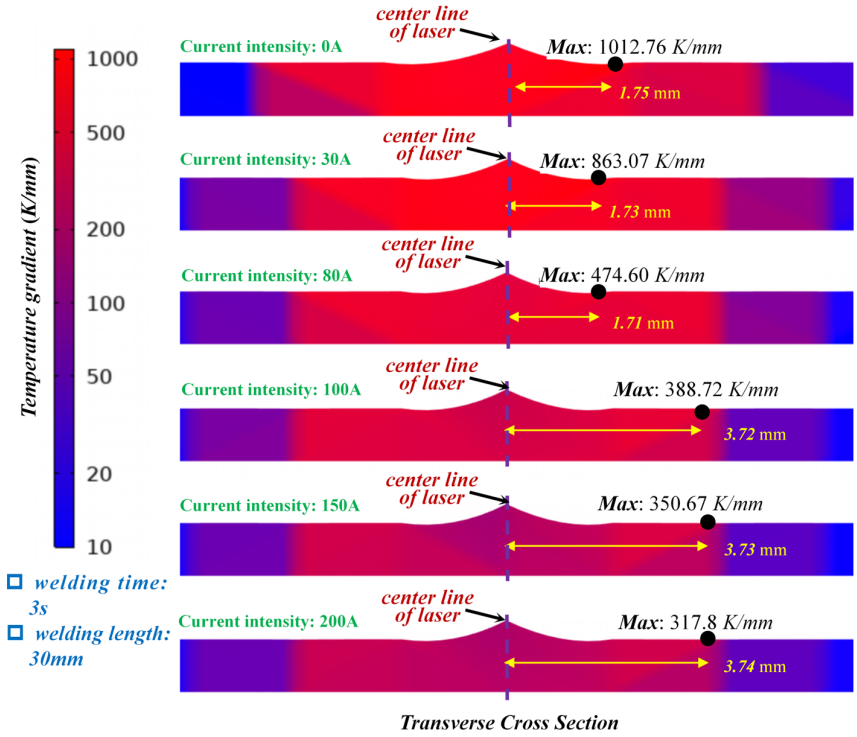


Figure 6. Temperature gradients in transverse cross section of melt pool with different electromagnetic field current intensities.

Compared to the application of directional static or pulse magnetic fields [13,15,20], the annular magnetic field generated by an external electromagnetic field generator can effectively relate the current intensity to the thermal dynamic behavior in the melt pool, such as the molten flow characteristics, temperature distribution, and temperature gradient. The changes in flow characteristics (from laminar flow to turbulence) and temperature gradient in the melt pool brought about by the increase of continuous and adjustable current intensities are clearly shown in the current work.

Based on the numerical results from the fluid thermodynamic modeling, the grain growth in the solidification of the melt pool of the laser-welded 316L steel plates could be simulated. When the time-dependent temperature distribution and melt flow velocity in the melt pool were considered in the Monte Carlo model, the changes in the grains in the transverse cross section could be well simulated (Figure 8). When the laser was moving across the measured transverse cross section in a welding time of 3.0 s, the largest melt pool boundary (i.e., solid–liquid interface) could be obtained (Figure 8b). Based on the nucleation rate calculations that considered undercooling, which was related to the melt flow velocity, new fine grains could be nucleated at the solid–liquid interface. They then grew into the melt pool, which was driven by the temperature gradient in the pool. When

there was no assistive electromagnetic field in the laser welding of 316L steel, the grain growth in the melt pool solidification process could be simulated in 646 Monte Carlo steps (MCS). To be more specific, when the welding time was 3.6 s, new nucleated fine grains could be found near the solid–liquid interface. In addition, many small equiaxial grains with a thickness of 0.396 mm could be found in the solidified region. For a welding time of 4.0 s, which was equivalent to 746 MCS, the thickness of the solidified region increased to 1.1 mm. More initial grains were then formed in the melt pool, and many small equiaxial grains grew larger. More specifically, small columnar grains could be found near the bottom of the melt pool. This was related to the epitaxial growth of the grains, which was driven by the temperature gradient. For a welding time of 5.0 s, which was equivalent to 996 MCS, the melt pool in the transverse cross section became filled with solid grains. Uniform equiaxial grains were then found in the top and middle of the melt pool, while small columnar grains were found near the initial melt pool boundary and the heat effect zone. Finally, when the welded plate cooled to ambient temperature, all equiaxial grains and columnar grains became coarsened.

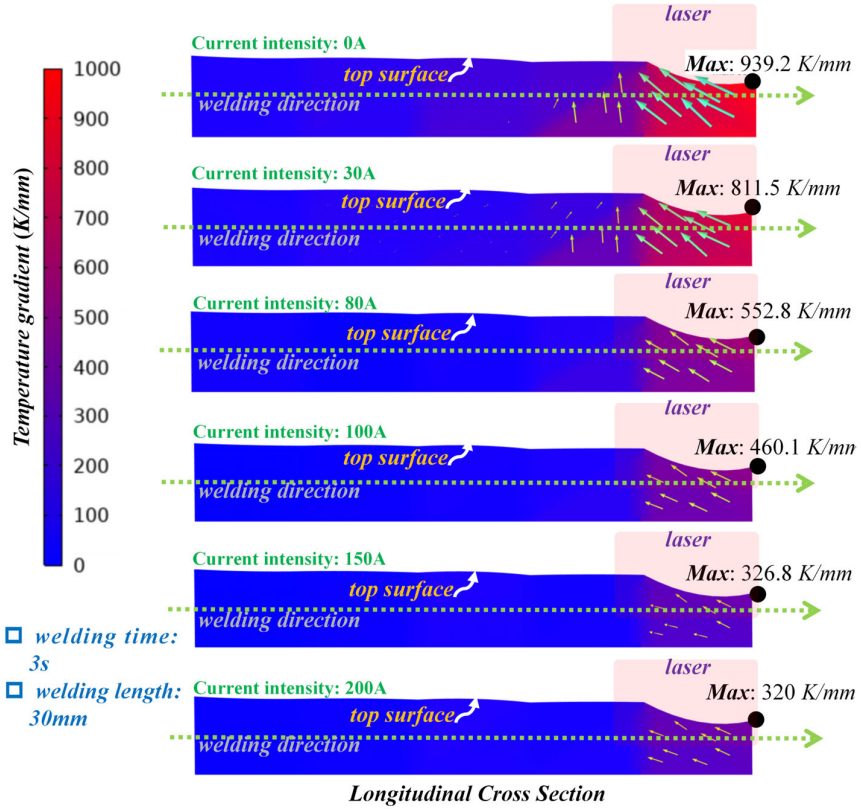
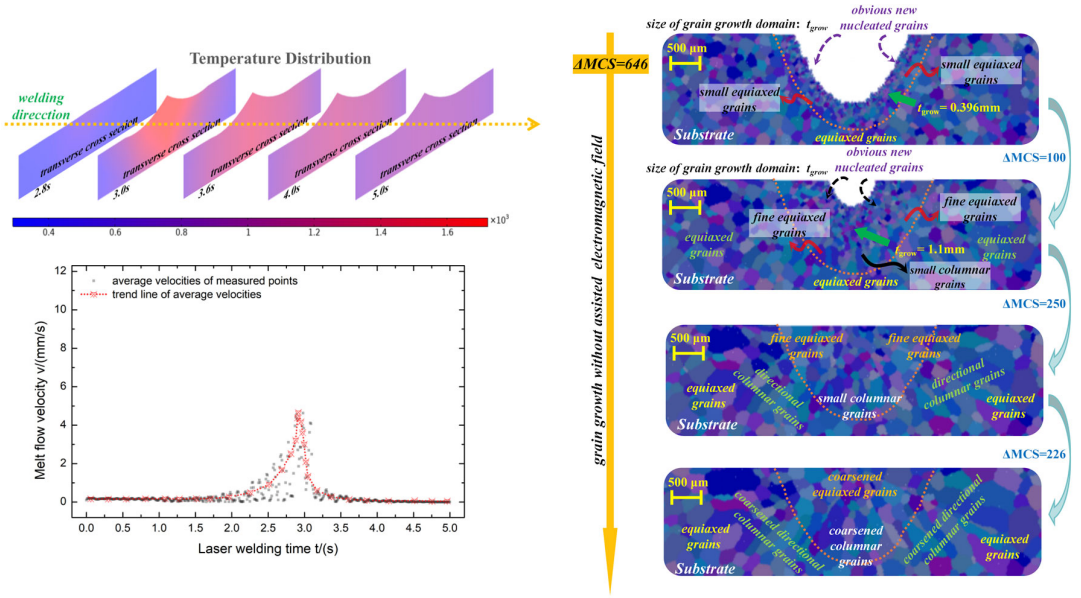


Figure 7. Temperature gradients and melt flow directions in longitudinal cross section of melt pool with different electromagnetic field current intensities.

As was the situation with the laser welding of 316L steel plates without an electromagnetic field, the temperature distribution and melt flow velocity were still the key factors for grain nucleation and growth during laser welding, even though an electromagnetic field with a current intensity of 30 A was used in this welding. When using a higher preheating temperature and before moving the laser across the cross section, the grains in the welded plate became slightly coarsened for a welding time of 3.0 s. The larger equiaxial grains in the substrate are presented in Figure 9b. For a welding time of 3.0 s, a melt pool of similar size was also found in the transverse cross section at almost the same maximum welding temperature. In addition, the undercooling in the melt pool decreased with a larger average melt flow velocity [49]. As a result, a smaller moving distance of the solid–liquid

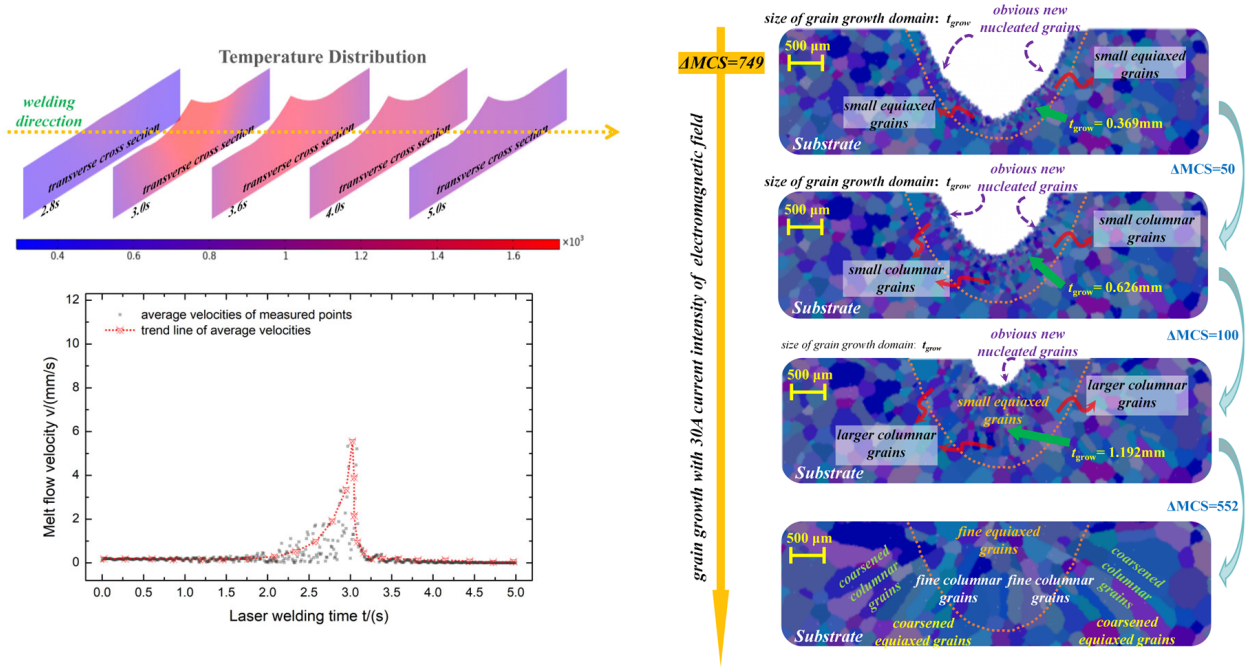
interface, the 0.369 increased solidification region thickness, was found after moving the laser in the forward direction for 0.6 s. For the same cooling time for the welded plates, the solidification time of the melt pool became greatly increased by the slower moving speed of the solid–liquid interface. Also, the size differences between the newly nucleated grains and the growing grains greatly increased, with a longer coarsening time for the growing grains. This led to a more pronounced epitaxial growth of the grains, which was driven by the temperature gradient. More and larger directional columnar grains were found in the transverse cross section (Figure 9). After cooling, only a small number of fine equiaxial grains was found near the top surface of the welded plates. In addition, many coarsened directional columnar grains were formed in the transverse cross section. This was advantageous for the increase in the mechanical properties of the laser-welded product but disadvantageous for the isotropic properties.



(**a**) (**b**)

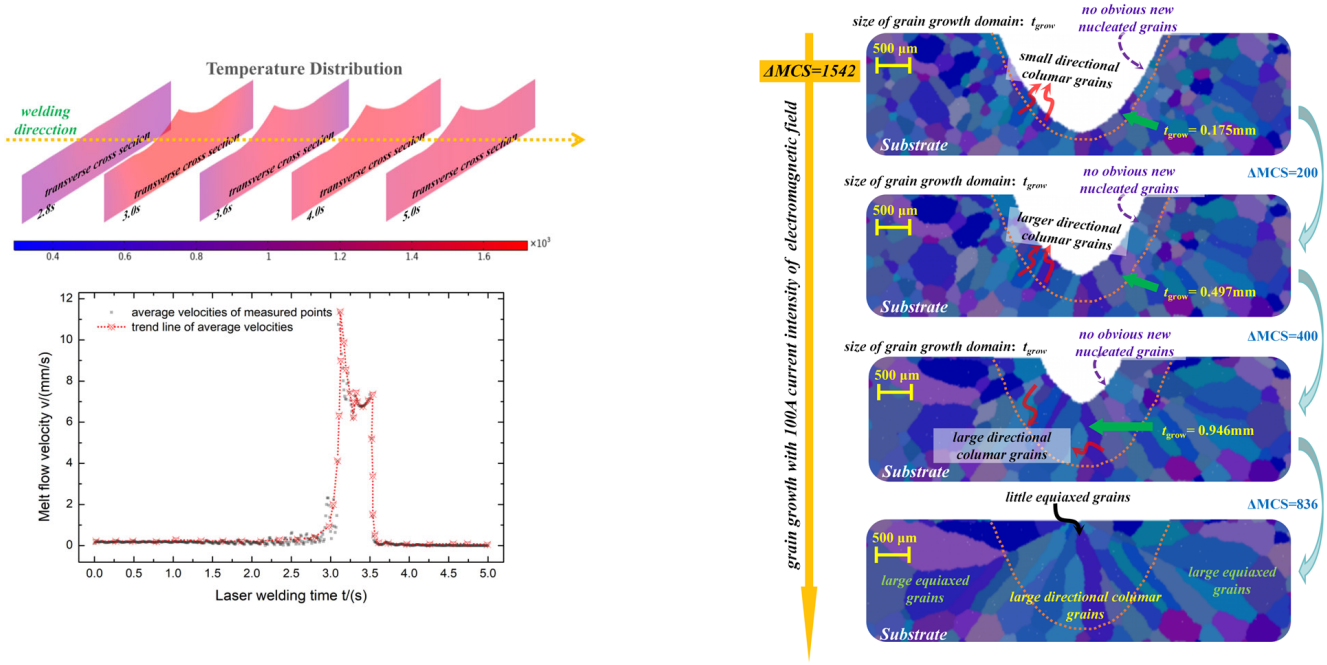
Figure 8. Grain growth considering the temperature distribution and melt flow in the melt pool of laser-welded 316L steel plate without assistive electromagnetic field: (**a**) the driven conditions of temperature and melt flow velocity in the Monte Carlo model; (**b**) grain growth process.

When an electromagnetic field with a current intensity of 100 A was used for laser welding, the higher temperature and faster melt flow velocity led to further coarsening of the grains in the transverse cross section (Figure 10). On the one hand, larger coarsened equiaxial grains were found in the substrate for which a higher preheating temperature was used before moving the laser across the cross section. On the other hand, the fast velocity in the melt pool resulted in the formation of turbulence. This led to a large decrease in the undercooling near the solid–liquid interface and, thereafter, to a decrease in the nucleation rate. When the assistive current intensity of the electromagnetic field was increased from 30 A to 100 and for a welding time increased by 0.6 s (from 3.0 s to 3.6 s), the thickness of the solidified region decreased from 0.369 mm to 0.175 mm, respectively. There were no clearly visible new nucleated grains at the interface (Figure 10b). Instead, they were consumed by the growing small directional columnar grains. With the cooling of the welded plate, the sizes of these directional columnar grains became increasingly larger. After the complete solidification of the welded 316L steel plate, small equiaxial grains were found in the transverse cross section and large directional columnar grains were found in the vicinity of this cross section.



(**a**) (**b**)

Figure 9. Grain growth considering the temperature distribution and melt flow in the melt pool of laser-welded 316L steel plate with assistive electromagnetic field (current intensity of 30 A): (**a**) the driven conditions of temperature and melt flow velocity in Monte Carlo model; (**b**) grain growth process.



(**a**) (**b**)

Figure 10. Grains growth considering the temperature distribution and melt flow in the melt pool of laser-welded 316L steel plate with assistive electromagnetic field (current intensity of 100 A): (**a**) the driven conditions of temperature and melt flow velocity in Monte Carlo model; (**b**) grain growth process.

To further study the effect of the current intensity of the electromagnetic field on grain growth in the transverse cross section, grain size analysis about the grain morphology and

size of the final grain morphology, which are listed in Tables 5–7, was performed using Monte Carlo simulations (Figures 11–13). For the situation with no assistive electromagnetic field in the laser welding, the main grain morphology within the transverse cross section consisted of equiaxial grains. The average size of the 41 equiaxial grains was 166.48 μm, with a maximum size of 330.94 μm and a minimum size of 81.65 μm. Also, there were more small-sized grains than large-sized ones (Figure 11b). Compared with the other grains, the length and width of the 27 columnar grains were much larger, with average sizes of 624.82 μm and 192.51 μm, respectively. The size distributions (length and width) of the columnar grains are presented in Figure 11b. For an electromagnetic field current intensity of 30 A, the main grain morphology within the transverse cross section changed into a columnar morphology. In the measured region, the melt pool and heat affected the zone. There were 46 observable grains, including 19 equiaxial grains and 27 columnar grains. The mean size of the equiaxial grains slightly decreased (from 166.48 μm to 165.01 μm) compared with the corresponding mean size obtained without an assistive electromagnetic field. Also, the columnar grains grew larger to a mean value of 773.5 μm. The maximum length and width of the coarsened columnar grains increased to 1270.57 μm and 652.06 μm, respectively. Thus, coarse grains could be obtained by using an electromagnetic field in the welding. When the assistive electromagnetic field current intensity increased to 100 A, the small equiaxed grains were all consumed by the large directional columnar grains. In the 17 observed columnar grains in the melt pool and heat-affected zone, the maximum length of the columnar grains was 1643.39 μm, which was 1.7 times larger than the maximum length obtained without an assistive electromagnetic field. Furthermore, the transverse cross section was full of coarsened directional columnar grains. Some columnar grains had even penetrated the thickness of the welded plate. In conclusion, an electromagnetic field can be used to obtain coarsened grains in the solidification of a laser-welded 316L steel plate. However, the applied current intensity needs to be controlled to prevent the overheating of the welded sample and the formation of turbulence. With control of the temperature distribution and melt flow velocity, the small equiaxed grains and columnar grains can all be coarsened to obtain the mechanical properties required in different industry applications.

Table 5. Grain sizes (without assistive electromagnetic field).

Grain Morphology	Max. Size	Min. Size	Mean Size	Num.
size of equiaxed grains r_{equ} (μm)	330.94	81.65	166.48	41
length of columnar grains l_{col} (μm)	972.25	316.77	624.82	27
width of columnar grains w_{col} (μm)	420.38	87.86	192.51	27

Table 6. Grain sizes (with 30A current intensity of assistive electromagnetic field).

Grain Morphology	Max. Size	Min. Size	Mean Size	Num.
size of equiaxed grains r_{equ} (μm)	295.74	112.13	165.01	19
length of columnar grains l_{col} (μm)	1270.57	323.4	773.5	27
width of columnar grains w_{col} (μm)	652.06	78.43	220.09	27

Table 7. Grain sizes (with 100A current intensity of assistive electromagnetic field).

Grain Morphology	Max. Size	Min. Size	Mean Size	Num.
size of equiaxed grains r_{equ} (μm)	-	-	-	-
length of columnar grains l_{col} (μm)	1643.39	801.41	1213.28	17
width of columnar grains w_{col} (μm)	515.39	142.34	264.83	17

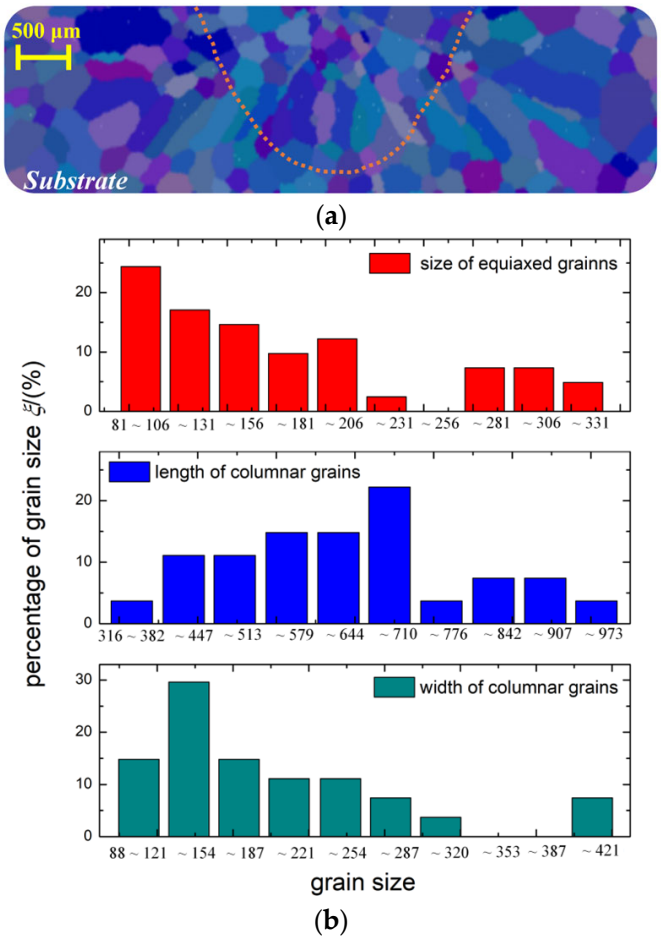


Figure 11. Morphology and grain size analysis of grains in transverse cross section of laser-welded 316L steel plate without assistive electromagnetic field: (**a**) final grain morphology in transverse cross section; (**b**) analysis results for grain numbers, size, and morphology.

In the current work, the directional growth of nucleated grains, considering a temperature gradient controlled by an assistive electromagnetic field, is simulated. In detail, the effect of the current intensity of an assistive electromagnetic field on grain morphology and size are discussed. It can be seen that, with an increase in melt flow velocity driven by the assistive electromagnetic field, an undercooling decrease leads to a longer nucleation time in the melt pool. More and larger directional columnar grains have then been formed after the consumption of small, nucleated grains near the solid–liquid interface. The mechanism that forms directional coarsened grains can be found in Refs. [50,51].

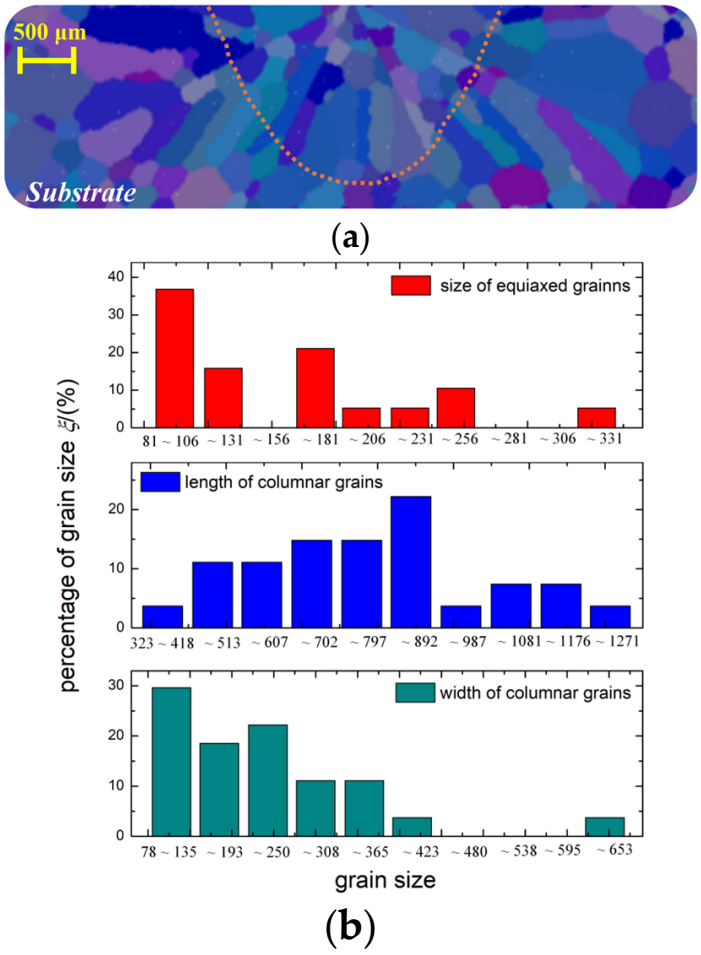


Figure 12. Morphology and grain size analysis of grains in transverse cross section of laser-welded 316L steel plate with assistive electromagnetic field (current intensity of 30 A): (**a**) final grain morphology in transverse cross section; (**b**) analysis results for grain numbers, size, and morphology.

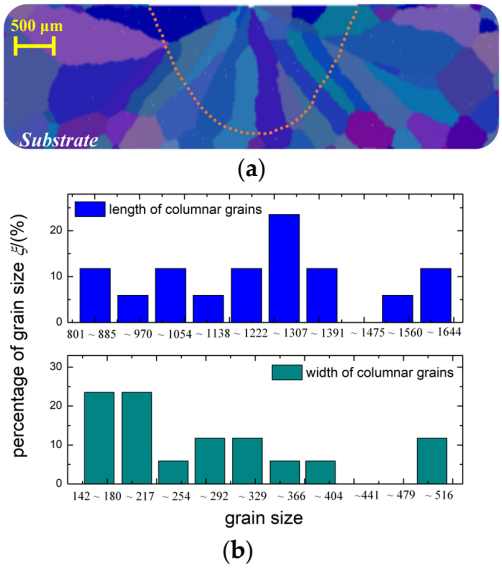


Figure 13. Morphology and grain size analysis of grains in transverse cross section of laser-welded 316L steel plate with assistive electromagnetic field (current intensity of 100 A): (**a**) final grain morphology in transverse cross section; (**b**) analysis results for grain numbers, size, and morphology.

5. Conclusions

To better understand the control of the microstructure in the laser welding of 316L steel with an assistive electromagnetic field, a thermal–electromagnetic hydrodynamic model has here been used in the study of the welding temperature and melt flow characteristics. In addition, grain growth during solidification was studied using the Monte Carlo model. By using this numerical model, which was appropriately verified by experimental data, including the temperature history and grain morphology, the impacts of the electromagnetic field current intensity on temperature distribution, melt flow characteristics, and grain growth during solidification were explored and discussed in some detail. The following conclusions can be drawn:

When an assistive electromagnetic field is used during laser welding, the Marangoni convection can be effectively controlled by the magnetic damping effect. The welding temperature can also be slightly increased by the electromagnetic heating effect. However, the applied current intensity of the electromagnetic field needs to be appropriately controlled to prevent the formation of an unstable turbulent flow and the overheating of the substrate.

The temperature gradient in the melt pool can be greatly decreased with the use of an assistive electromagnetic field. In the present study, the temperature gradient could be decreased by 13.5% by controlling the temperature distribution and melt flow velocity in the laminar flow in the melt pool. In the turbulent flow, and with the use of an assistive current intensity of 100 A, the temperature gradient in the melt pool could even be decreased by more than 50%.

The undercooling decrease, which is caused by an increase in the melt flow velocity with the use of an assistive electromagnetic field, leads to a longer nucleation time in the melt pool. More and larger directional columnar grains are then formed after the consumption of small, nucleated grains near the solid–liquid interface, which was driven by the force of the temperature gradient. With control of temperature distribution and melt flow velocity, the required grain morphology (equiaxial grains or columnar grains) and dimensions (radius, length, or width) can be controlled by a coarsening and epitaxial growth. For example, if coarsened columnar grains are the needed grain morphology, the maximum current intensity of the assistive electromagnetic field to produce the required temperature gradient decrease and homogenization of molten material is 30 A.

Author Contributions: Validation, Z.Z., X.X., P.G. and K.L.; Investigation, Z.Z., X.X. and P.G.; Data curation, Z.Z. and X.X.; Writing—original draft, Z.Z.; Writing—review & editing, Z.Z., X.X., P.G. and K.L. All authors have read and agreed to the published version of the manuscript.

Funding: This study is funded by the Machinery Technology Development Fund of China National Institute [108YJ2022003, Peng Ge], the Postdoctoral Science Foundation of China [2022M712921, Peng Ge], and the Frontier Technologies R&D Program of Jiangsu [BF2024047, ZhengWei Zhang].

Data Availability Statement: The original contributions presented in this study are included in the article. Further inquiries can be directed to the corresponding author.

Conflicts of Interest: Author Peng Ge was employed by the company Zhengzhou Research Institute of Mechanical Engineering Co., Ltd. The remaining authors declare that the research was conducted in the absence of any commercial or financial relationships that could be construed as a potential conflict of interest.

References

1. Ke, W.C.; Bu, X.Z.; Oliveira, J.P.; Xu, W.G.; Wang, Z.M.; Zeng, Z. Modeling and numerical study of keyhole-induced porosity formation in laser beam oscillating welding of 5A06 aluminum alloy. *Opt. Laser Technol.* **2021**, *133*, 106540.
2. Sun, R.J.; Li, L.H.; Zhu, Y.; Guo, W.; Peng, P.; Cong, B.Q.; Sun, J.F.; Che, Z.G.; Li, B.; Guo, C.; et al. Microstructure, residual stress and tensile properties control of wire-arc additive manufactured 2319 aluminum alloy with laser shock peening. *J. Alloys Compd.* **2018**, *747*, 255–265. [CrossRef]
3. Zhang, C.; Yan, Y.; Cong, C.; Zeng, X.Y.; Gao, M. Suppressing porosity of a laser keyhole welded Al-6Mg alloy via beam oscillation. *J. Mater. Process. Technol.* **2020**, *278*, 116382. [CrossRef]
4. Hojjatzadeh, S.M.H.; Parab, N.D.; Guo, Q.L.; Qu, M.L.; Xiong, L.H.; Zhao, C.; Escano, L.I.; Fezzaa, K.; Evehart, W.; Sun, T.; et al. Direct observation of pore formation mechanisms during LPBF additive manufacturing process and high energy density laser welding. *Int. J. Mach. Tools Manuf.* **2020**, *153*, 103555.
5. Zhang, Y.; Chen, G.Y.; Wei, H.Y.; Zhang, J. A novel "sandwich" method for observation of the keyhole in deep penetration laser welding. *Opt. Lasers Eng.* **2008**, *46*, 133–139.
6. Meng, X.M.; Bachmann, M.; Artinov, A.; Rethmeier, M. A study of the magnetohydrodynamic effect on keyhole dynamics and defect mitigation in laser beam welding. *J. Mater. Process. Technol.* **2022**, *307*, 117636.
7. Zhao, C.; Parab, N.D.; Li, X.X.; Fezzaa, K.; Tan, W.D.; Rollett, A.D.; Sun, T. Critical instability at moving keyhole tip generates porosity in laser melting. *Science* **2020**, *370*, 1080–1086.
8. Ai, Y.W.; Liu, X.Y.; Huang, Y.; Yu, L. Numerical investigation of pore defect formation in the weld during high speed laser welding. *J. Laser Appl.* **2020**, *32*, 022066.
9. Ai, Y.W.; Jiang, P.; Wang, C.M.; Mi, G.Y.; Geng, S.N. Experimental and numerical analysis of molten pool and keyhole profile during high-power deep-penetration laser welding. *Int. J. Heat Mass Transf.* **2018**, *126*, 779–789.
10. Khan, M.S.; Ali, S.; Westerbaan, D.; Duley, W.; Biro, E.; Zhou, Y.N. The effect of laser impingement angle on the optimization of melt pool geometry to improve process stability during high-speed laser welding of thin-gauge automotive steels. *J. Manuf. Process.* **2022**, *78*, 242–253.
11. Squillace, A.; Prisco, U.; Cillberto, S.; Astarita, A. Effect of welding parameters on morphology and mechanical properties of Ti-6Al-4V laser beam welded butt joints. *J. Mater. Process. Technol.* **2012**, *212*, 427–436. [CrossRef]
12. Farida, B.; Boualem, S.; Amin, M.M.E.I.; Benali, B. 3-D finite element analysis of stress concentration factor in spot-welded joints of steel: The effect of process-induced porosity. *Comput. Mater. Sci.* **2011**, *50*, 1450–1459.
13. Du, D.F.; Haley, J.C.; Dong, A.P.; Fautrelle, Y.; Shu, D.; Zhu, G.L.; Li, X.; Sun, B.D.; Lavernia, E.J. Influence of static magnetic field on microstructure and mechanical behavior of selective laser melted AlSi10Mg alloy. *Mater. Des.* **2019**, *181*, 107923. [CrossRef]
14. Chen, J.C.; Wei, Y.H.; Zhan, X.H.; Li, Y.; Ou, W.M.; Zhang, T. Melt flow and thermal transfer during magnetically supported laser beam welding of thick aluminum alloy plates. *J. Mater. Process. Technol.* **2018**, *254*, 325–337. [CrossRef]
15. Kao, A.; Gan, T.; Tonry, C.; Krastins, I.; Pericleous, K. Thermoelectric magnetohydrodynamic control of melt pool dynamics and microstructure evolution in additive manufacturing. *Philos. Trans. R. Soc. A* **2020**, *378*, 20190249. [CrossRef]
16. Fautrelle, Y.; Wang, J.; Salloum-Abou-Jaoude, G.; Abou-Khalil, L.; Reinhart, G.; Li, X.; Ren, Z.M.; Nguyen-Thi, H. Thermo-electric-magnetic hydrodynamics in solidification: In situ observations and theory. *JOM* **2018**, *70*, 764–771. [CrossRef]
17. Guo, S.; Zhao, Y.F.; Sui, S.; Zhu, P.C.; Wang, M.; Hao, X.H.; Song, Y.L.; Guo, A.F.; Ni, J.J.; Qin, Y.B.; et al. Effect of static magnetic field on the chemical short-range order of CoCrFeMnNi high-entropy alloy prepared by laser powder bed fusion. *Intermetallics* **2024**, *175*, 108498. [CrossRef]
18. Sun, W.; Liu, S.S.; Guo, F.Q.; Wu, D.T.; Zhang, Y.G.; Zou, Y. Investigation on droplet transfer behavior during fiber laser-flux cored arc hybrid welding. *Opt. Laser Technol.* **2022**, *148*, 107781. [CrossRef]
19. Shoichi, M.; Yukio, M.; Koki, T.; Yasushi, T.; Yukinori, M.; Yusuke, M. Study on the application for electromagnetic controlled molten pool welding process in overhead and flat position welding. *Sci. Technol. Weld. Join.* **2013**, *18*, 38–44. [CrossRef]
20. Zhou, J.; Tasai, H.L. Effects of electromagnetic force on melt flow and porosity prevention in pulsed laser keyhole welding. *Int. J. Heat Mass Transf.* **2007**, *50*, 2217–2235. [CrossRef]
21. Xu, D.; Liu, X.S.; Wang, P.; Yang, J.G.; Fang, H.Y. New technique to control welding buckling distortion and residual stress with non-contact electromagnetic impact. *Sci. Technol. Weld. Join.* **2009**, *14*, 753–759. [CrossRef]
22. Meng, X.M.; Bachmann, M.; Artinov, A.; Rethneier, M. Experimental and numerical assessment of weld pool behavior and final microstructure in wire feed laser beam welding with electromagnetic stirring. *J. Manuf. Process.* **2019**, *45*, 408–418. [CrossRef]
23. Li, J.Z.; Liu, Y.B.; Kang, K.X.; Sun, Q.; Jin, P.; Liu, Y.; Cai, C.W.; Sun, Q.J. A novel approach to regulate energy allocation and melt flow in narrow gap laser welding with electromagnetic assisted wire wobbling. *J. Mater. Process. Technol.* **2021**, *289*, 116909. [CrossRef]
24. Su, Z.L.; Yin, L.M.; Jiang, H.; Zhang, L.; Chen, Y.H.; Zhang, L.P.; Zhang, H.H.; Feng, W. Research progress of electromagnetic pulse welding technology: A review. *J. Mater. Res. Technol.* **2025**, *36*, 217–235. [CrossRef]

25. Deng, F.X.; Wnag, Y.; Liu, F.M.; Li, D.J.; Jiang, C. Analysis and experiment of flat electromagnetic pulse welding process based on magnetic field shaper. *Int. J. Adv. Manuf. Technol.* **2025**, *137*, 5611–5623. [CrossRef]
26. Wu, C.S.; Yang, F.Z.; Gao, J.Q. Effect of external magnetic field on weld pool flow conditions in high-speed gas metal arc welding. *Proc. Inst. Mech. Eng. Part B J. Eng. Manuf.* **2016**, *230*, 188–193. [CrossRef]
27. Zhang, H.; Wang, Q.J.; Wang, G.D.; Ding, H.F. Analytical modeling and optimization design of an electromagnetic pulse welding device with a field shaper for metal plates. *IEEE Access* **2020**, *8*, 187721–187729. [CrossRef]
28. Chen, X.; Luo, M.; Hu, R.Z.; Li, R.D.; Liang, L.J.; Pang, S.Y. Thermo-electromagnetic effect on weld microstructure in magnetically assisted laser welding of austenite steel. *J. Manuf. Process.* **2019**, *41*, 111–118. [CrossRef]
29. Shuai, S.S.; Lin, X.; Xiao, W.Q.; Yu, J.B.; Wang, J.; Ren, Z.M. Effect of transverse static magnetic field on microstructure of Al-12% Si alloys fabricated by powder-blow additive manufacturing. *Acta Metall. Sin.* **2018**, *54*, 918–923.
30. Nie, J.W.; Chen, C.Y.; Shuai, S.S.; Liu, X.Q.; Zhao, R.X.; Wang, J.; Liao, H.L.; Ren, Z.M. Effect of static magnetic field on the evolution of residual stress and microstructure of laser remelted Inconel 718 superalloy. *J. Therm. Spray Technol.* **2020**, *29*, 1410–1423. [CrossRef]
31. Wang, L.; Yan, W.T. Thermoelectric magnetohydrodynamic model for laser-based metal additive manufacturing. *Phys. Rev. Appl.* **2021**, *15*, 064051. [CrossRef]
32. Zeng, C.; Huang, F.; Xue, J.T.; Jia, Y.; Hu, J.X. Effect of combined direct current electric field and pulsed magnetic field on the transient melt pool in laser additive manufacturing process. *3D Print. Addit. Manuf.* **2023**, *11*, e1887–e1898. [CrossRef] [PubMed]
33. Azimzadegan, T.; Mousavi, S.A.A.A. Microstructure and solidification cracking analysis of dissimilar pulsed laser welded hastelloy X to 347 stainless steel using phase-field models. *Metall. Mater. Trans. B* **2021**, *52*, 2307–2326. [CrossRef]
34. Geng, S.N.; Jiang, P.; Shao, X.Y.; Guo, L.Y.; Gao, X.S. Heat transfer and fluid flow and their effects on the solidification microstructure in full-penetration laser welding of aluminum sheet. *J. Mater. Sci. Technol.* **2020**, *46*, 50–63. [CrossRef]
35. Elmesalamy, A.S.; Abdolvand, H.; Walsh, J.N.; Francis, J.A.; Suder, W.; Williams, S.; Li, L. Measurement and modelling of the residual stresses in autogenous and narrow gap laser welded AISI grade 316L stainless steel plates. *Int. J. Press. Vessel. Pip.* **2016**, *147*, 64–78. [CrossRef]
36. Unni, A.K.; Muthukumaran, V. Numerical simulation of the influence of oxygen content on the weld pool depth during activated TIG welding. *Int. J. Adv. Manuf. Technol.* **2021**, *112*, 467–489. [CrossRef]
37. Xu, G.X.; Li, P.F.; Cao, Q.N.; Hu, Q.X.; Gu, X.Y.; Du, B.S. Modelling of fluid flow phenomenon in laser+GMAW hybrid welding of aluminum alloy considering three phase coupling and arc plasma shear stress. *Opt. Laser Technol.* **2018**, *100*, 244–255. [CrossRef]
38. Zhao, W.Y.; Wei, Y.H.; Long, J.W.; Chen, J.C.; Liu, R.P.; Ou, W.M. Modeling and simulation of heat transfer, fluid flow and geometry morphology in GMAW-based wire arc additive manufacturing. *Weld. World* **2021**, *65*, 1571–1590. [CrossRef]
39. Zhou, X.F.; Cao, X.B.; Zhang, F.; Duan, J.A. Numerical and experimental investigation of thermal stress distribution in laser lap welding of Ti6Al4V and 2024 alloy plates. *Int. J. Adv. Manuf. Technol.* **2022**, *118*, 1427–1440. [CrossRef]
40. Ross, A.J.; Bitharas, I.; Perkins, K.G.; Moore, A.J. Volumetric heat source calibration for laser powder bed fusion. *Addit. Manuf.* **2022**, *60*, 103267. [CrossRef]
41. Ge, W.J.; Han, S.; Fang, Y.C.; Cheon, J.; Na, S.J. Mechanism of surface morphology in electron beam melting of Ti6Al4V based on computational flow patterns. *Appl. Surf. Sci.* **2017**, *419*, 150–158. [CrossRef]
42. Ge, W.J.; Fuh, J.Y.H.; Na, S.J. Numerical modelling of keyhole formation in selective laser melting of Ti6Al4V. *J. Manuf. Process.* **2021**, *62*, 646–654. [CrossRef]
43. Katzarov, I.; Malinov, S.; Sha, W. Finite element modeling of the morphology of β to α phase transformation in Ti-6Al-4V alloy. *Metall. Mater. Trans. A* **2002**, *33*, 1027–1040. [CrossRef]
44. Ge, P.; Zhang, Z.; Tan, Z.J.; Hu, C.P.; Zhao, G.Z.; Guo, X. An integrated modeling of process-structure-property relationship in laser additive manufacturing of duplex titanium alloy. *Int. J. Therm. Sci.* **2019**, *140*, 329–343. [CrossRef]
45. Zhang, Z.; Ge, P.; Li, J.Y.; Ren, D.X.; Wu, T. Monte Carlo simulations of solidification and solid-state phase transformation during directed energy deposition additive manufacturing. *Prog. Addit. Manuf.* **2022**, *7*, 671–682. [CrossRef]
46. Zhang, Z.; Wang, Y.F.; Ge, P.; Wu, T. A Review on modelling and simulation of laser additive manufacturing: Heat transf, microstructure evolutions and mechanical properties. *Coatings* **2022**, *12*, 1277. [CrossRef]
47. Zhang, Z.; Tan, Z.J.; Yao, X.X.; Hu, C.P.; Ge, P.; Wan, Z.Y.; Li, J.Y.; Wu, Q. Numerical methods for microstructural evolutions in laser additive manufacturing. *Comput. Math. Appl.* **2019**, *78*, 2296–2307. [CrossRef]
48. Sheikhbahaee, H.; Pakmanesh, M.R.; Mirahmadi, S.J.; Asghari, S. Investigating governing parameters influencing solidification process in pulsed laser micro-welding of AISI 316L thin foils using finite element method. *Int. J. Adv. Manuf. Technol.* **2021**, *116*, 1819–1830. [CrossRef]
49. Yu, Y.F.; Wang, L.; Zhou, J.; Li, H.X.; Li, Y.; Yan, W.T.; Lin, F. Impact of fluid flow on the dendrite growth and the formation of new grains in additive manufacturing. *Addit. Manuf.* **2022**, *55*, 102832. [CrossRef]

50. Pu, J.; Chen, T.M.; Rao, J.W.; Sun, Y.B.; Chen, Y.X.; Jiang, C.H.; Sun, H.W. Study on the microstructure and properties of Al alloy/steel CMT welding-brazing joints under different pulse magnetic field intensities. *Coatings* **2024**, *14*, 1515. [CrossRef]
51. Hu, C.; Wang, C.M.; Ma, X.Q.; Zhu, Z.W.; Jiang, P.; Mi, G.Y. EBSD study on magnetic field altering crystal texture and grain growth during laser-hybrid welding. *Mater. Des.* **2022**, *216*, 110587. [CrossRef]

Disclaimer/Publisher's Note: The statements, opinions and data contained in all publications are solely those of the individual author(s) and contributor(s) and not of MDPI and/or the editor(s). MDPI and/or the editor(s) disclaim responsibility for any injury to people or property resulting from any ideas, methods, instructions or products referred to in the content.